Send Orders for Reprints to reprints@benthamscience.ae

Current Pharmaceutical Design, 2016, *22*, 000-000

Technological Innovations in Magnetic Resonance for Early Detection of Cardiovascular Diseases

M.F. Santarelli[1,2], V. Positano[1,2], N. Martini[2], G. Valvano [3] and L. Landini[1,2,3]

[1]*CNR Institute of Clinical Physiology, 56124 Pisa, Italy;* [2]*Fondazione G. Monasterio, CNR-Regione Toscana, 56124 Pisa, Italy;* [3]*Department of Information Engineering, University of Pisa, 56124 Pisa, Italy*

M.F. Santarelli

Abstract: Most recent technical innovations in cardiovascular MR imaging (CMRI) are presented in this review. They include hardware and software developments, and novelties in parametric mapping. All these recent improvements lead to high spatial and temporal resolution and quantitative information on the heart structure and function. They make it achievable ambitious goals in the field of magnetic resonance, such as the early detection of cardiovascular pathologies.

In this review article, we present recent innovations in CMRI, emphasizing the progresses performed and the solutions proposed to some yet opened technical problems.

Keywords: Cardiovascular magnetic resonance imaging (CMRI), accelerated CMRI, cardiac ultrahigh field MRI, parametric mapping, T1 mapping, T2 mapping, T2* mapping, tagging, 4D flow MRI, cardiac MRS.

INTRODUCTION

Cardiovascular magnetic resonance imaging (CMRI) has become a valuable diagnostic imaging modality in the non-invasive detection of cardiovascular diseases.

The field of CMRI has evolved rapidly over the past decade, feeding new applications across a broad spectrum of clinical and research areas [1-5], such as global and regional cardiac function, myocardial perfusion, myocardial viability, tissue characterization, and proximal coronary anatomy.

CMRI provides a plenty of high resolution, high quality, quantitative information on the heart structure and function. Advantages of CMRI include its lack of ionizing radiation, its ability to image the entire heart regardless of the orientation and shape of the heart and vessels, and its ability to produce different contrasts according to different physiological mechanisms.

Emerging CMRI techniques now enable multi-parametric *in vivo* characterization of the heart, from changes in global heart structure and function, to changes in tissue composition and mechanics.

Thanks to the recent technical innovations, real-time CMRI is becoming a reality [6], offering dynamic imaging of the heart and major vessels with high spatial and temporal resolution.

In this review article, we present recent innovations in CMRI, emphasizing the progresses performed and the solutions proposed to some yet opened technical problems.

FROM 1.5TESLA TO ULTRA HIGH FIELDS: HARDWARE AND SOFTWARE DEVELOPMENTS

One of the main purposes of the current CMRI systems, dictated by physiological motion and flow, is tracking and visualization of rapidly moving cardiac structures using dynamic imaging of the heart, covering the entire cardiac cycle. Such feature is of great clinical relevance for the assessment of cardiac morphology and function. This requires high temporal resolution, high muscle/blood contrast, full coverage of the cardiac cycle and short scan times.

*Address correspondence to this author at the Institute of Clinical Physiology, National Research Council (CNR), Via Moruzzi 1, 56124, Pisa, Italy; E-mail: santarel@ifc.cnr.it

Several solutions have been proposed recently for obtaining such objectives, and involve both hardware and software developments. As far as the hardware novelties are concerned, they include the current clinical use of high field MR systems (1.5T - 3.0Tesla) [7-9], moving towards ultra-high field MR (UHF-MR) i.e. B0 $\geq$ 7.0 Tesla, [10-12], with the consequent development of the other hardware components such as multichannel radiofrequency (RF) transmit and receive coils [13-15] , and novel gating and triggering technologies [10, 16].

Continuous movement towards higher field MR is mainly due to several advantages that, at least theoretically, can be obtained. Firstly, the increased magnetic field strength results in a theoretical linear increase in the signal-to-noise ratio (SNR) [17]. Secondly, increasing the magnetic field strength increases frequency separation of off-resonance spins; this leads to an increase of the frequency difference between various hydrogen-based compounds. The enhanced frequency differences may be exploited for improvement in contrast-to-noise ratio (CNR), spectroscopic imaging and potentially in fat suppression [18-20]. Thirdly, increasing the main magnetic field increases the T1 of many tissues, with a negligible effect on the T2. The increase in T1 can have beneficial effects in some applications such as myocardial tagging and myocardial tissue characterization [7, 8, 21, 22]. Finally, imaging speed and efficiency can be obtained in higher field strength with suitable pulse sequences and acquisition parameters settings. Such advantages are more pronounced in UHF-MR.

Unfortunately, to date, in the face of the advantages, there are also physics related unpleasant phenomena and practical obstacles to be taken into account. Some problems to be addressed are: magnetic field inhomogeneity, off-resonance artifacts, dielectric effects and RF non-uniformities, localized tissue heating and RF power deposition constraints, and synchronization of data acquisition with the cardiac cycle using conventional ECG [23]. All of these effects can weaken the benefits of high-field strengths, and reduce the image quality of CMRI. Luckily, some successful strategies for solving or reducing technical weaknesses are proposed in the literature and used in clinical data. Among them, the use of multichannel transmit/receive coils and accelerated MR imaging strategies, appear to be the most promising and efficient solutions.

1381-6128/16 $58.00+.00

Multichannel Transmit/Receive Surface Coils

Multichannel RF transmission technique can solve problems relevant to: 1. dielectric effects on tissue, leading to local/regional signal inhomogeneities or signal voids: and 2. increased and locally focused RF power deposition (quantified as specific absorption ratio, SAR) that can cause local tissue heating [24, 25]. Moreover, multichannel receive coils reduce distortions caused by susceptibility artefacts, allowing faster imaging and higher spatial resolutions [26].

So that, the combination of transmit/receive (also called transceiver) multiple coils is considered a good new technique for increasing MR images quality and speedup. Recently, several transceiver cardiac coil arrays are designed and built specifically for cardiac studies, especially for UHF-MR systems, where more signal inhomogeneities and high SAR value are present [27-30]. One of the features of transmit/receive multichannel coils for cardiac studies, is their geometries: coil elements must cover the chest wall, towards the left, the sensitive region must be large enough to cover the cardiovascular anatomy. Also, the number of coil elements greatly varied among the proposed multichannel transceiver coils: they vary from 4 to 32 elements for 7 T MR systems [23, 31] the increase in the number of elements increases the field of view, can potentially improve the SNR and/or increase the imaging speed, but at the expense of difficulties in the design and realization of the coils system, and transmission and reception data processing.

Multidimensional arrangement of the coil elements enables multidimensional accelerations, reduces acquisition time, and results in patient's comfort. In fact, as in multichannel receive coil it is possible to exploit the so called parallel imaging greatly accelerating the MRI acquisition time, also distinct RF excitation waveforms may be used as a means of accelerating RF pulses; such new technique is usually called 'transmit parallel imaging' or 'transmit SENSE' [32].

Other applications of parallel transmit MRI take an approach that has been called '$B1^+$ shimming' [10, 33], which improves the homogeneity of the transmit component of the RF magnetic field. Therefore, by the combined use of multichannel coils in transmission and reception, high resolution and fast imaging can be obtained.

ACCELERATED MRI

Recently, new software techniques have been developed aimed to accelerate MR data acquisition.

The MR scanner acquires data in a Fourier domain called *k-space*; in conventional MR data acquisition such scanning operation is time consuming. Among the accelerated MRI techniques, non-uniform data sampling methodology is greatly used [34, 35], but at the expense of time consuming reconstruction. Compressive sensing (CS) allows to reduce the scanning time by sampling the k-space below the Nyquist sampling rate [36, 37]. The basic idea of CS technique is that, it is sufficient to have a small number of random linear combinations of the signal values for defining a compressible signal. In fact, the first CS requisite is that the signal is sparse or compressible, i.e. it can be represented with few non zero coefficients in a certain transformation domain [38]. This requisite is usually met in MRI images, since they are compressible in different domains, like the Wavelet domain. The second requisite is that the coherence of the aliasing artifacts, resulting from the undersampling, is incoherent. A random subset of Fourier coefficients met this second constraint; so, CS appears to be able to make accurate reconstructions from a small subset of k-space rather than an entire k-space grid. The first application of CS in MRI was described in [38], where the acceleration strategy was based on incoherent undersampling of phase-encodes.

Different sampling strategies have been proposed during the years in order to achieve a better image quality. In Cartesian imaging, a commonly used sampling strategy is the Poisson disk sampling [39, 40]. It allows for a random variable density sampling, characterized by low coherence of the aliasing artifacts. However, the sampling pattern achieved with a random subset of the phase encoding points is far from that ideally required by CS. This can result in a smaller achievable acceleration. Better acquisition strategies are represented by non Cartesian trajectories, like spirals [39, 41, 42].

CS has been successfully applied in dynamic CMRI, exploiting k-t space sparsity [43, 44]. In [43] a new algorithm called k-t FOCUSS (*k-t* space FOCal Underdetermined System Solver) is described, that can successfully reconstruct a high resolution cardiac sequence even from severely limited k-t samples, without incurring aliasing artifacts often observed in conventional methods.

A further acceleration technique recently applied on MR data exploits the low-rank property of matrices, instead of simple sparsity of vectors. In fact, the temporal frames of a dynamic dataset are highly correlated, and this results in low rank property of the matrix representing the dynamic dataset. This technique has started to gain interest in dynamic MRI [45], and was recently applied on 3D flow [46], 3D tagging [47], and 3D perfusion [48].

Because sparsity and low-rankness are complementary properties, methods have been proposed recently which combine the CS and low-rankness methods [49-51].

All the acceleration techniques described above, can be combined with the parallel imaging methodology. In the recent literature, several studies are described that combine CS and parallel imaging [52-56]. The multichannel CS method simultaneously uses data from the multiple channels to reconstruct the desired image instead of reconstructing separate images from each channel, resulting in higher acceleration factors and improved image quality [55].

In [57] a novel method is described, that integrates fast scanning, parallel imaging, and both low-rank and sparse modeling. This integration of accelerating techniques, allows the achievement of high-speed cardiac imaging, with high spatial resolution. In fact, authors applied such combined techniques on 3D rat cardiac imaging at 67 fps and 0.65 mm × 0.65 mm × 0.31 mm spatial resolution and on 2D human cardiac imaging up to 22 fps and 1.0 mm × 1.0 mm spatial resolution, without the use of ECG gating, respiratory gating, or breath holds. This is the evidence that the MR real time imaging at high spatial resolution is close to reality and no longer a goal.

T1, T2 AND T2* PARAMETRIC MAPPING

Recent developments in CMRI enable rapid parametric mapping of myocardial tissue assessing its relaxation properties (T1, T2, and T2* relaxation times) [58]. To generate a relaxation map, multiple images of the heart are acquired varying the time of acquisition, and the signal intensities of these images are fit to a mathematical model which describes the underlying relaxation phenomenon. Relaxation mapping typically involves acquisition of multiple images within a single breath-hold and thus requires fast acquisition techniques.

T1 Mapping

Myocardial T1 relaxation time is altered in a variety of pathological processes like edema, fibrosis, and lipid and iron deposition. In particular, compared with healthy volunteers, T1 values were found to be lower in iron-overload [59] and Anderson-Fabry disease patients [60], while increased T1 values are reported in acute and chronic myocardial infarction [61], myocarditis [62] and amyloidosis [63]. Currently, T1 mapping is considered one of the most important biomarker in the diagnosis of myocardial diffuse fibrosis which is difficult to detect using solely the standard late gadolinium enhancement (LGE) technique [64]. Furthermore, T1 mapping is a fundamental tool for the quantification of the extracellular volume

(ECV) in the myocardium, another important biomarker of interstitial disease [65]. ECV maps are derived from pre-contrast T1 values, also called native T1, and post-contrast T1 values of the myocardium and the blood pool, and corrected for hematocrit [66].

Several methods have been proposed for myocardial T1 mapping, all based on inversion/saturation preparation pulses and acquisition of single-shot images during the recovery of the longitudinal magnetization. The modified Look-Locker Inversion recovery (MOLLI) [67] uses three inversion pulses each followed by single-shot acquisitions triggered at a fixed cardiac phase in successive heartbeats. A pictorial representation of the MOLLI sequence scheme is shown in Figure **1**. The single-shot acquisition is performed with balance steady state free precession (b-SSFP) readout. In the original version of MOLLI, the number of images acquired after each of the three inversion pulses is three, three and five, respectively (3-3-5 scheme), yielding a total of eleven images, each sampled at a different inversion time (TI). A resting period of three heartbeats is inserted before the second and the third inversion pulse to allow the recovery of the longitudinal magnetization. T1 estimation is then obtained through pixelwise fitting using a three-parameter-monoexponential model which accounts for the perturbation of the longitudinal magnetization during the SSFP readout. Since the fitting procedure is applied to magnitude data, multiple fittings are usually performed to assign the correct polarity to the images with shortest TI [68]. Recently, a phase sensitive inversion recovery (PSIR) reconstruction has been proposed to restore signal polarity without increasing the computational cost [69]. In addition, non-rigid motion correction of MOLLI images before fitting has proven to be a valuable tool to increase the robustness and the accuracy of T1 mapping [70].

A number of modifications of the original MOLLI protocol have been introduced by varying the number of acquired images [71], their corresponding TI [72] and the duration of the resting periods [73] with the aim of shortening the acquisition time or improving the accuracy or precision in T1 estimation. Alternative approaches like Saturation recovery Single Shot Acquisition (SASHA) [74] utilize a saturation preparation, or a combination of saturation and inversion preparations as introduced by Saturation Pulse Prepared Heart rate independent Inversion-Recovery (SAPPHIRE) [75]. Each method has its benefits and drawbacks in terms of accuracy, precision, and overall reproducibility (for complete review, see refs [76-78]). In general, T1 estimation is affected by off-resonances, imperfect saturation or inversion, heart rate, magnetization transfer, fitting model and pulse sequence parameters. This variability has induced the T1-mapping working group to provide a set of recommendations for reproducible image acquisition, quantitation, and reporting of T1 and ECV measurement [79]. Having control of the influencing factors mentioned above, T1 and ECV mapping can be considered sufficiently robust to be used in clinical settings. Recently, there are increasing number of studies which validate fibrosis measurement derived from T1 and ECV mapping with histology-derived assessment of collagen volume fraction [80-82], which confirmed the central role of these techniques as prognostic tool in myocardial fibrosis [83].

T2* Mapping

Quantification of T2* value in the heart is likely the most clinically established parametric characterization technique as it allowed the early detection and monitoring of cardiac iron burden [84]. To create a myocardial T2* map, gradient echo images at different TEs are acquired, leading to signal intensities following a T2* relaxation curve (Fig. **2**). The most commonly used MR sequence is a multiecho segmented gradient echo sequence that collect data at 8-10 TEs, starting from the minimum TE allowed on the scanner (about 2 ms). The TE interval is usually set to 2.26 ms to minimize the effect of signal oscillation due to the chemical shift effect on the fat-water interface, leading to a typical TEs ranging from 2 ms to 20-24 ms [85]. Images are acquired after the R-wave in an interval of about 200 ms to minimize the effect of blood flow and heart motion. The major problem in T2* heart imaging is represented by magnetic susceptibility artefacts induced by deoxygenated blood in cardiac veins and by the heart-lung interface, that are particularly

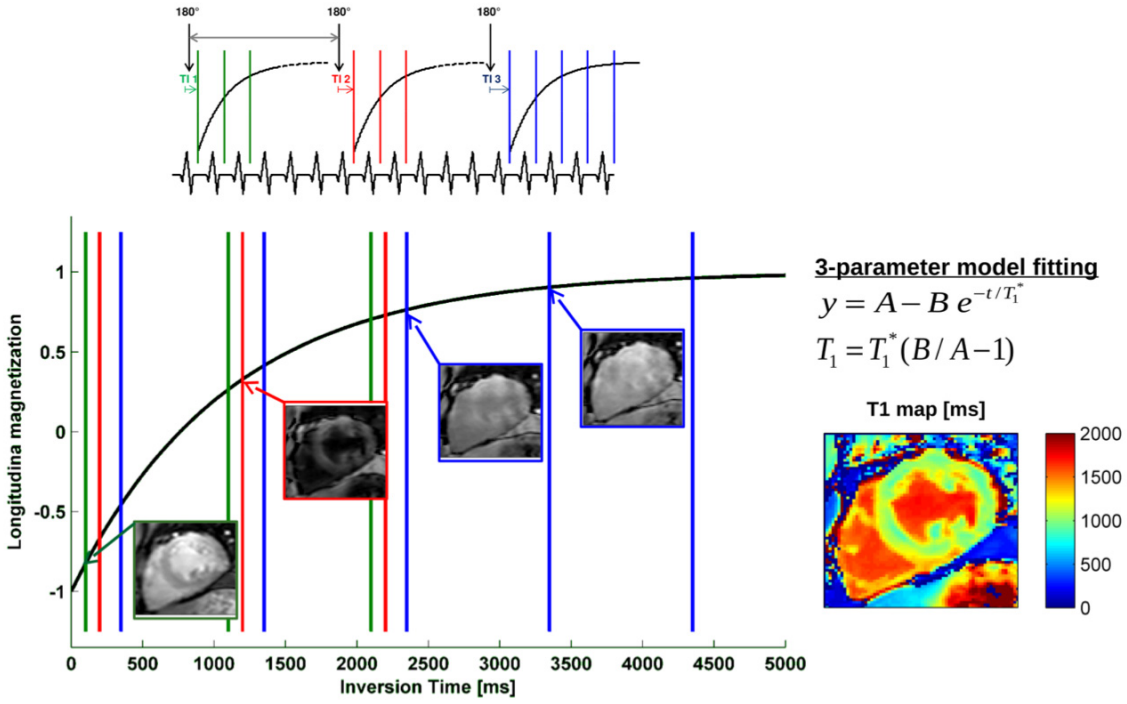

Fig. (1). Pictorial representation of the myocardial T1 mapping using the MOLLI method.

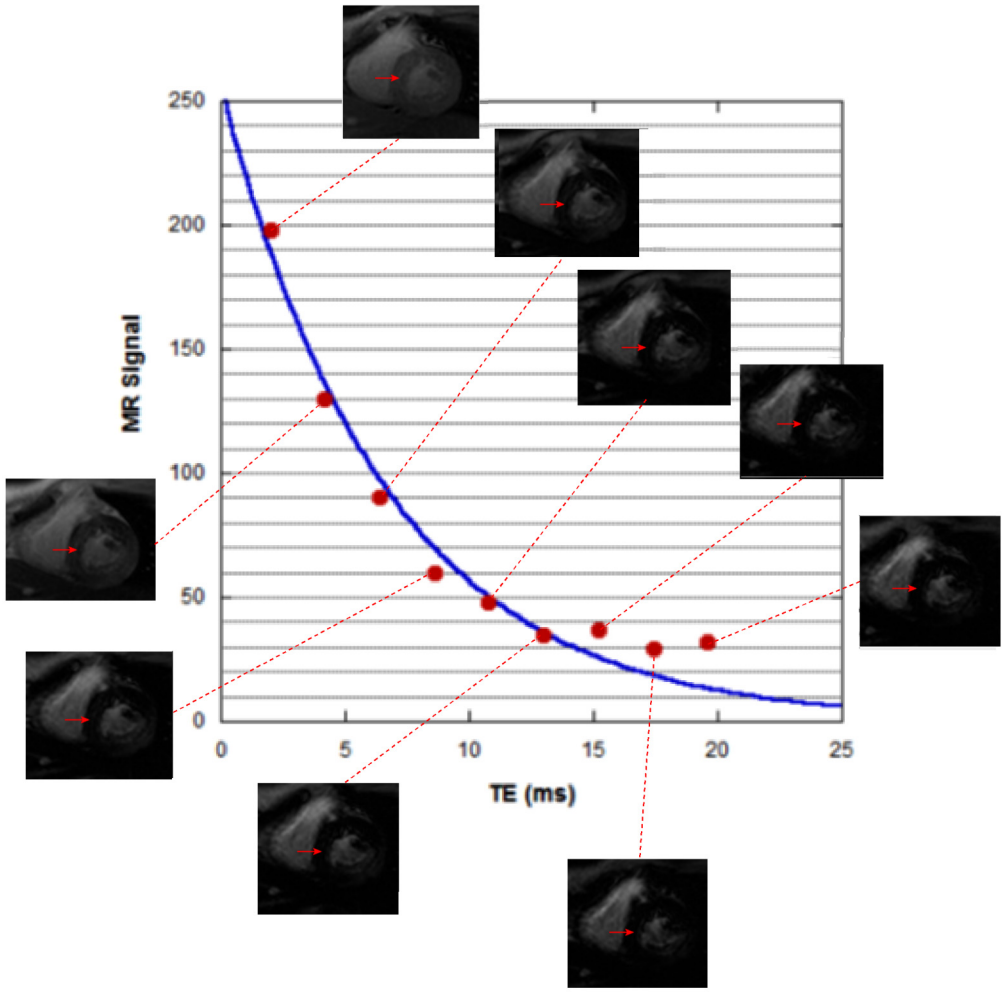

Fig. (2). Exemplification of the T2/T2* mapping procedure.

evident at later TEs [85]. For this reason T2* measurements for iron overload assessment are commonly done in the intra-ventricular septum as this area is typically free from magnetic susceptibility artifacts, although the analysis could be extended to the whole myocardium if an appropriate artefacts correction strategy is employed [86] allowing segmental monitoring of iron overload progression [87]. As T2* value in case of severe iron overload dramatically decreases becoming few ms, the signal rapidly disappears and the effect of noise cannot be neglected, leading to a signal decay that diverges from the theoretical pure exponential decay model at later TEs (see Fig. **2**).

Two main approaches have been proposed to address this issue in the computation of T2* maps. The first (truncation model) consists of automatically limiting the mono-exponential equation to few echo times [88]. The second consists of a non-linear fitting of the signal to an exponential plus a constant offset model that compensates for the noise plateau [89]. Both approaches may be challenging regarding computation time, as direct calculation of T2* value is not possible, as it happens by using the pure exponential model.

Figure **3** shows T2* heart map obtained from a normal subject in (a), and from a thalassemia major patient with severe cardiac iron overload in (b).

As previously pointed out, detection and measurement of cardiac iron overload represents the main clinical application of quantitative T2* mapping. T2* mapping was also applied to characterize myocardial hemorrhage in acute myocardial infarction [90]. T2* mapping could be also used in blood oxygenation level dependent (BOLD) studies to assess the presence of oxygenated blood in the cardiac wall. In principle, a reduction of the T2* value is expected in left ventricle (LV) regions supplied by a stenotic coronary artery, so a rest-stress T2* approach could be used to assess coronary artery disease (CAD) without the need of a contrast medium as in MR perfusion studies [91].

T2* mapping was successfully performed in 3T [92] and 7T scanners [93]. The fact that the T2* value linearly decreases with the static magnetic field [93] discourages the use of high-field scanners in iron overload assessment as low T2* values associated with severe iron burden cannot be effectively measured. Instead, the use of high-field scanner may be preferable in BOLD studies as the reduction of the expected T2* value increase the effectiveness of the MR acquisition sequence [91].

T2 Mapping

Quantitative measurement of the myocardial T2 relaxation time has important advantages over the standard T2 weighted (T2-W) semiquantitative technique, that presents some intrinsic limitations as regional variations in signal intensity from coil inhomogeneities and the need to define a “remote” myocardium region as reference. T2 mapping is typically achieved by acquiring dark-blood or black-blood spin-echo images with different echo times yielding images with signal intensities that follow a T2 decay curve. Dark-blood

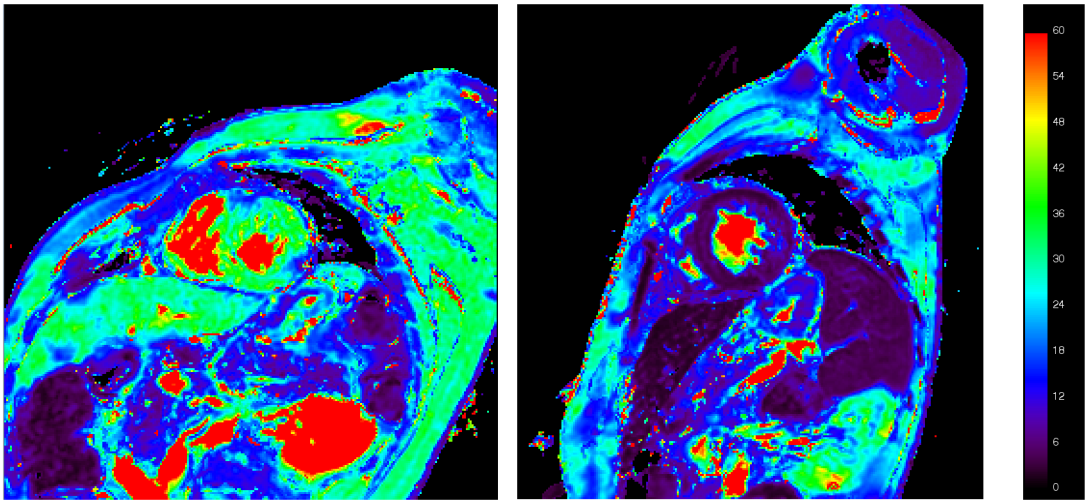

Fig. (3). Heart T2* maps of a normal subject (a, myocardial T2* about 35 ms) and a patient with severe cardiac iron overload (b, myocardial T2* value about 5 ms).

images are usually acquired by turbo-spin-echo (TSE) sequences, while bright-blood images are acquired by T2 magnetization-preparation (T2-prep) sequences exploiting rapid collection of data by a non-cartesian k-space sampling [94]. Fast acquisition techniques as TSE or T2-prep are associated with an overestimation (about 10%) of T2 values with respect to a pure spin-echo technique due to mixed T2 and T1 relaxation effect [95]. In general, sequence acceleration techniques adopted to fit the constraints posed by cardiac imaging are likely to induce systematic errors in T2 values assessment [96]. On the other hand, a too long acquisition time may be not sustainable for the patient and could lead to artefacts in the resulting T2 map due to cardiac motion [97]. Hence, acquisition time represents the most challenging point in the introduction of T2 mapping technique in the clinical practice. As myocardial T2 values are high enough with respect to TEs used in the acquisition, the fitting of signal decay curve is usually done to a single exponential decay model neglecting the effect of MR noise [97], so the computation of T2-maps is usually faster and simpler with respect to T2*-maps. Figure **4** shows a spin-echo multiecho acquisition of the heart and the resulting T2 map.

T2 mapping techniques could be useful for the evaluation of a variety of cardiac pathologies. The most important application is the detection and assessment of myocardial edema and inflammatory diseases, as T2 increases in the edematous myocardium [58]. T2 mapping was also proposed for myocardial iron-overload evaluation, as the presence of iron reduces the T2 value [98].

HEART WALL STRAIN AND STRAIN RATE EVALUATION (TAGGING)

Early myocardial dysfunction can be effectively detected by CMRI, improving risk stratification for developing heart failure (HF). Assessment of global ventricular function by CMRI allows toevaluate useful diagnostic indices, as ejection fraction, that are strong predictors of future HF. However, global measures may miss regional heart function dysfunction. Thus, accurate quantification of myocardial strain and torsion could help to detect subclinical myocardial dysfunction. Currently, CMRI tagging represents the "gold standard" for assessment of heart regional function [99].

Myocardial tissue tagging was firstly introduced in 1988 [100]. Noninvasive markers (tags) are created before image acquisition in the myocardial tissue by locally induced perturbations of the magnetization with selective radiofrequency saturation of tag planes perpendicular to the imaging plane. As these perturbations correspond to low signal intensity regions they appear as dark lines. Later, the spatial modulation of magnetization (SPAMM) technique allowed defining tags in two orthogonal directions obtaining a grid of myocardial tissue markers [101]. More recently, parallel imaging techniques, such as simultaneous acquisition of spatial harmonics (SMASH) [102] and sensitivity encoding (SENSE) [103], have been applied to tagging sequences to minimize the image acquisition time allowing reduction of the breath-hold time, or increase of spatial resolution for the same breath-hold duration. The main problem in tagging acquisition is represented by tag lines fading during cardiac cycle, due to T1 relaxation, that limits its application to the systolic part of the cycle. This problem can be mitigated by using high field strength (i.e. 3T), obtaining a better CNR improving at the same time tags persistence [106].

CMRI tagging image analysis can be performed by segmentation and tracking of tagging lines as in Findtags [107] and SPAMMVU methods [108]. Alternative methods adopt an optical flow-based approach that assesses motion by detecting the spatial and temporal changes of image intensity. The most widely used approach is harmonic phase (HARP) analysis, based on processing of phase images [109]. In the HARP approach, tagging images are decomposed into a harmonic magnitude and a harmonic phase. Tagging data are extracted by filtering the harmonic peaks in the frequency domain. A strain map is obtained by tracking the phase changes of tag lines through the cardiac cycle. The HARP approach is highly automated and, thus, limits both analysis time and operator induced variability.

CMRI tagging is usually performed in the short axis view, although acquisition of long axis cardiac planes would allow more sophisticated three dimensional (3D) strain analysis. Several 3D model-based approaches were proposed to reconstruct the 3D motion of the left ventricle by tagging images [110]. However, these methods are poorly applicable in clinical practice due to the high number of breath holds required and image misalignment induced by patient motion and heart rate variability.

The typical results of image analysis include measurement of strain, computed as the ratio between the reference fiber length (usually measured in tele-diastolic phase) and the fiber length during cardiac cycle, and the strain rate measured as the time derivatives of strain. Both indices are typically measured in the radial direction (toward the center of LV) and in the circumferential direc-

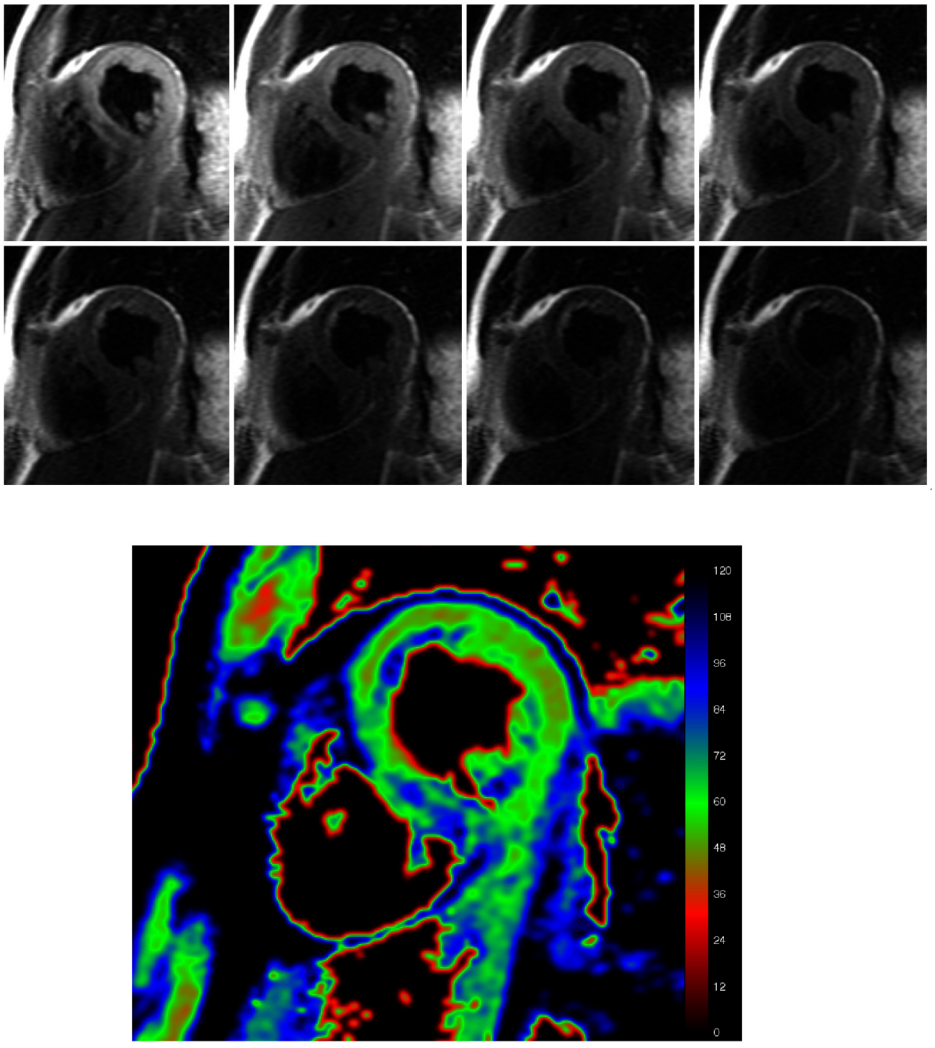

Fig. (4). SE multiecho images of the heart (TEs=6, 22, 39, 56, 73, 90, 106, 123 ms) and the corresponding T2 map.

tion (tangential to epicardial surface). If a 3D approach is employed, longitudinal strain and strain rate can be assessed along the LV long axis.

CMRI tagging was successfully applied to early detection of silent CAD in asymptomatic populations [111, 112]. The tagging technique could also be used in study of non-ischemic cardiomyopathies, as non-ischemic dilated (DCM) and Hypertrophic cardiomyopathies (HCM) [113]. Finally, CMRI tagging represents a unique tool to study ventricular dyssynchrony and to select patients that could benefit from cardiac resynchronization therapy (CRT).

4D FLOW MRI

Phase Contrast Magnetic Resonance Imaging (PC-MRI) is a well-established technique used to visualize and quantify the pulsatile blood flow in the human vascular system. The PC-MRI technique is based on the concept of velocity encoding, i.e. the use of bipolar gradients to obtain a linear relationship between the blood velocity and the phase of the MR signal. In standard 2D cine PC-MRI, a series of velocity maps are collected during the cardiac cycle with velocity encoding in through-plane direction. This technique is commonly used in clinical setting to quantify the blood flow in the heart, aorta and great vessels. 4D flow MRI is the extension of 2D cine PC-MRI to volumetric coverage and three-directional velocity encoding along three orthogonal directions [114]. Figure **5** shows an example of magnitude and velocity datasets obtained with 4D flow MRI of the thoracic aorta.

4D flow acquisitions require long scan times for typical cardiovascular applications, ranging from 5 to 20 minutes depending on heart rate, spatio-temporal resolution and anatomic coverage [115]. To reduce scan times, spatiotemporal parallel imaging methods [116, 117] and efficient k-space sampling patterns [118, 119] are usually adopted. In thoracic and abdominal applications, respiratory motion compensation strategies are needed to reduce breathing artifacts. In the respiratory navigator technique, the 4D flow scan is interleaved with the acquisition of a small volume at liver-lung interface which is used to estimate the respiratory phase [[120]]. Otherwise, in self-navigation approaches the breathing phase is estimated directly from the central profiles of the k-space [121].

Post-processing of 4D flow data typically includes the phase correction due to eddy currents and gradient non-linearity and the generation of the angiogram dataset (PC-MRA), given by the combination of magnitude and velocity data, which particularly highlights the vascular anatomy. A key benefit of 4D flow MRI is that, flow quantification can be performed a posteriori at user selected 2D planes positioned in the vessels of interest [122].

Furthermore, 4D flow MRI permits the visualization and quantification of 3D blood flow, thus providing a unique opportunity to reveal abnormal hemodynamic patterns [123]. Different visualiza-

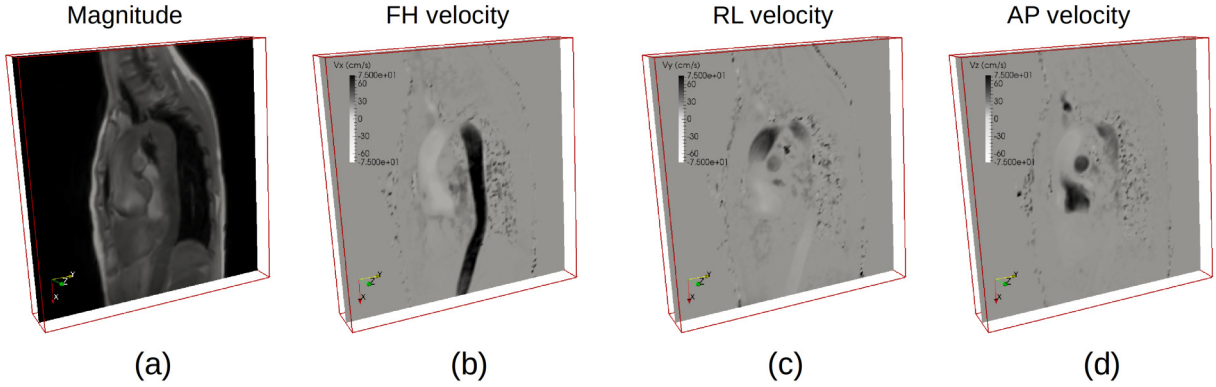

Fig. (5). 4D flow MRI acquisition of the thoracic aorta. (**a**) Magnitude and velocity datasets in feet-head (**b**) right-left (**c**) anterior-posterior (**d**) directions respectively.

tion strategies are commonly used to depict 3D blood flow patterns. Vector graphs show the magnitude and the direction of the blood velocity at each voxel, streamlines represent instantaneous tangents to velocity vectors at a specific time, and pathlines or 3D particle traces represent the actual trajectories followed by flow particles over time. Color-coding by velocity magnitude is also adopted to identify high velocity regions [115]. Figure **6** shows an example of 3D visualization of 4D flow MRI dataset of the aorta.

Besides qualitative assessment given by the 3D visualization of the blood flow, 4D flow MRI has been used by several authors to derive quantitative hemodynamic parameters such as outflow asymmetry [124], wall shear stress [125], pulse wave velocity [126], flow helicity [123], pressure difference mapping [127] and viscous energy loss [128], among others.

In the recent years, 4D flow MRI technique has been demonstrated to be a valuable tool in a large number of cardiovascular applications. In particular, 4D flow MRI of the thoracic aorta has been successfully applied in the study of aortic valve disease [129], aortic valve stenosis [130], aortic coarctation [131] and aortic dissection [132].

MRS, MRSI AND NOT-PROTON IMAGING

Magnetic resonance spectroscopy (MRS) is an accurate, non-invasive, non-ionizing tool for *in vivo* cardiac metabolism evaluation [133]. Thanks to the repeatability of the measurements, changes in cardiac metabolism during the (early) development of disease or during the follow-up can be assessed.

In the literature, a recent review [134] is presented that accurately describes the strengths and weaknesses of MRS from various nuclei (^{1}H, ^{31}P, ^{13}C) for evaluating cardiac metabolism. As highlighted in the paper, the cardiac MRS technique is not currently used in clinical practice, mainly for problems of acquisition times, spatial resolution, and low SNR. However, thanks to the new hardware and software techniques, such as those shown in the preceding paragraphs, these obstacles could be overcome soon and the potential of the cardiac MRS can also be exploited in clinical practice.

Most magnetic resonance spectroscopy studies are based on the detection of signals from a single volume by using the well-established single-voxel (SV) localization techniques. With these techniques the signal is received from a three dimensional volume of interest (VOI) with high field homogeneity across the volume. In cardiac MRS, the VOI is placed in the interventricular septum to avoid signal contamination from blood and pericardial fat. Single volume localization techniques are unable to detect the heterogeneous distribution of the content of metabolite across the VOI. To overcome this limitation, several magnetic resonance spectroscopic imaging (MRSI) techniques have been developed in order to acquire localized spectra from a multidimensional array of locations [134, 136]. MRSI, also called chemical shift imaging (CSI), is based on the phase encoding concept used in MRI for spatial localization. The total acquisition time in CSI is proportional to the number of voxels to be encoded. Although conventional CSI is the optimal technique in terms of sensitivity per unit time [137], the long acquisition times limited the application *in vivo*.

The RF coil for ^{1}H-MRS is usually the same RF coil used as for MRI. RF volume coils are mostly used for signal transmission because of their high B1 field homogeneity and can also be employed as receive coils. Cardiac ^{1}H-MRS studies in humans are usually performed using surface receive-only coils, obtaining a higher SNR. ^{31}P-MRS, ^{13}C-MRS and 23Na-MRI require dedicated coils and an additional (multi-nuclei) RF channel. For ^{31}P- and ^{13}C-MRS studies, usually surface coils are used as transmit/receive coils [138-140].

Moreover, using multi-channel coils or phased-array receive coils, SNR can be further improved in cardiac MRS [134, 141]. Multichannel coils also enable parallel imaging, thereby reducing the scan time, and consequently, the duration of cardiac examinations [142].

In the following section, the potentialities of the ^{1}H, ^{31}P, ^{13}C and ^{23}Na MRS and MRI techniques for cardiac metabolism study, and solution proposals to some technical limits, are briefly reported.

^{1}H-MRS

Proton magnetic resonance spectroscopy (^{1}H-MRS) allows the measurement of the content of human myocardial triglycerides (TGs), whose accumulation has been linked to cardiac dysfunction [143], and total creatine (Cr) content, whose depletion has been observed in the failing heart [144].

The main technical issue that has limited the use of ^{1}H-MRS in the clinical practice is that MR spectra are characterized by low SNR, because the concentration of cardiac metabolites is several orders of magnitude lower than water. One solution to this drawback is averaging of multiple acquisitions, but at the expense of increased scan times. The use of phased array radio frequency (RF) coils has been shown to be an effective way to improve the SNR of cardiac ^{1}H spectra without prolonging scan times [134, 145].

In cardiac 1H-MRS, as in other nuclei MRS, cardiac and respiratory movements are another cause of spectral quality degrading due to: moving spins during localizing gradients, outer voxel contamination, and B_0-field inhomogeneity. The use of ECG triggering and respiratory navigator techniques was shown to significantly increase the reproducibility of ^{1}H-MRS in the human heart 146, 147].

A fast alternative to ^{1}H-CSI is the echo planar spectroscopic imaging (EPSI) technique, in which oscillating gradients during

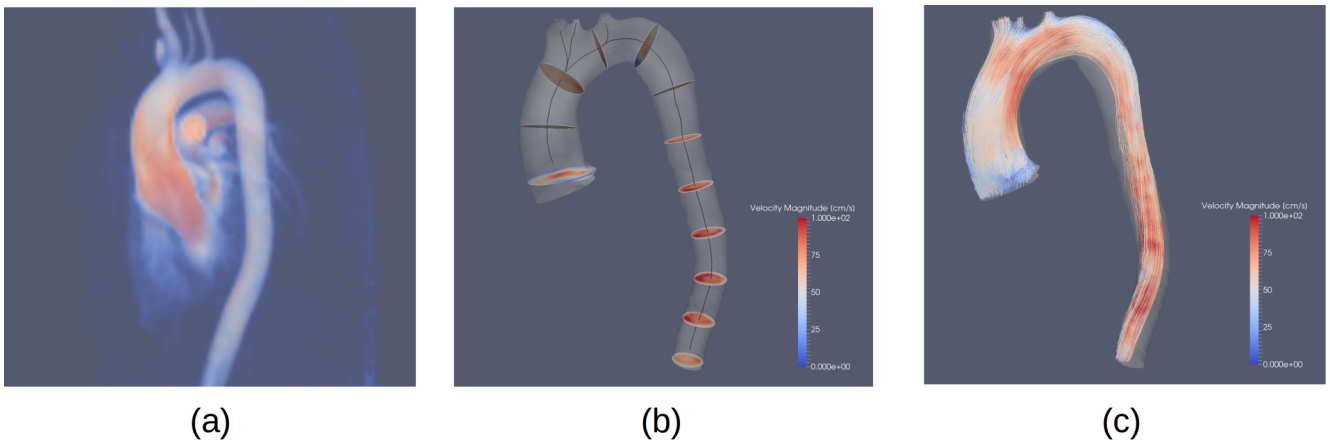

Fig. (6). 4D flow MRI of the thoracic aorta. (**a**) Volume rendering of the PC-MRA dataset. (**b**) Visualization of the segmented aortic wall and velocities on 2D planes distributed along the vessel centerline. (**c**) Visualization of 3D particle traces.

signal acquisition encode simultaneously the spatial and the spectral dimension. This dramatically reduces acquisition time since phase encoding steps in one spatial direction are eliminated. Recently, the EPSI technique has been successfully implemented for mapping the spatial distribution of TG and Cr content in the *in vivo* heart during free breathing acquisitions [136].

^{31}P-MRS

Phosphorus magnetic resonance spectroscopy (^{31}P-MRS) allows the non-invasive measurement of adenosine triphosphate (ATP) and phosphocreatine (PCr), high-energy phosphate metabolites that play a fundamental role in cardiac metabolism [18, 148].

The relative MR sensitivity of phosphorus is about 15 times lower than that of a proton. However, there is no dominant signal that requires suppression to detect the peaks of interest (such as the water signal in ^{1}H-MRS).

The ratio between PCr and ATP has been largely used to characterize altered energy metabolism. A review of clinical research results of cardiac ^{31}P-MRS studies was recently presented in [134].

There are two main limitations concerning the measurement of PCr/ATP ratios. Firstly, simultaneous alterations of both metabolites cannot be detected by relative ratios. Secondly, contamination of blood signal results in underestimation of PCr/ATP values. At a 1.5-T scanner, it has been shown that the PCr/ATP ratios using 3D localization techniques (3D image-selected *in vivo* spectroscopy (ISIS), and a combination of 2D ISIS and 1D CSI) are comparable, but significantly lower PCr/ATP ratios are obtained using 1D CSI [134, 149]. The lower PCr/ATP ratio with the less well-defined localization by 1D CSI may be a result of contamination of cardiac spectra by liver tissue and/or skeletal muscle, or by contamination of blood, which would add ATP signals, but no PCr [134]. An efficient method, called 'spatial localization with optimal point spread function' (SLOOP), was developed [150], which incorporates anatomical prior knowledge obtained from MRI scans. The SLOOP method is able to adapt the acquisition volume to anatomical structures with arbitrary shapes, and to incorporate experimental parameters into the model to yield absolute concentrations. SLOOP improves the localization in ^{31}P-MRS, with reduced contamination from adjacent organs; compared with CSI, the SNR was improved by approximately 30% [151]. Moreover, the absolute quantification has the advantage that it is unaffected by concentration changes of the reference metabolite.

^{13}C-MRS

In the recent years, a new methodology based on MRS using hyperpolarized ^{13}C appears very useful for studying cardiac metabolism in animal models [152-156]. This is due to the wide range of compounds that can be detected and the ability to attribute signals to the different carbon atoms within individual molecules. Hyperpolarization technique is used to enhance nuclear polarization, allowing increased MR signal intensity. In *in vivo* cardiac applications, mainly dynamic nuclear polarization (DNP) technique is used for polarising the interested 13C nuclei [157]. After generating the hyperpolarized sample, it is rapidly melted and, subsequently, it is injected or infused. After administration of the hyperpolarized sample, it is metabolized and the ^{13}C label is transferred to other metabolites, which can be monitored. The high SNR provided by the hyperpolarized ^{13}C technique allows both the visualization of the injected molecule and also the downstream metabolic products to which the ^{13}C label is transferred.

The hyperpolarized ^{13}C-labeled tracers are normal physiologically occurring compounds such as ^{13}C-pyruvate [158, 159], ^{13}C-acetate [160], ^{13}C-lactate [160]. The main feature of this methodology relies on *in vivo* measurement of metabolism non-invasively and without radiation exposure. Preliminary cardiovascular studies on experimental animals appear promising [162, 163].

23Na -MRI

The sodium (^{23}Na) and potassium (^{39}K) exchange between the intracellular and extracellular space plays an important role in living tissue. The supply with energy in the form of ATP and its hydrolysis cause the sodium-potassium pump (Na+-K+-ATPase) to maintain Na+ and K+ concentration gradients across the cell membrane. An ATP deficiency leads to a breakdown of the pump mechanism, which results in an increase in intracellular sodium concentration. ^{23}Na MRI can be considered as a valid instrument for tissue viability studies in living tissues, including the heart [164].

Sodium nucleus has a lower *in vivo* concentration and sensitivity respect to proton. Moreover, 23Na has a lower gyromagnetic ratio than proton (≈25% of ^{1}H). The signal from *in vivo* sodium in myocardium is then about 12,000 times lower than proton signal. Consequently, ^{23}Na imaging suffers from poor SNR and increased scan times. A result of the lower gyromagnetic ratio is that the B1 field required to induce nutation needs to be higher (about the double). SAR increases proportionately as the square of the peak RF utilized; therefore, SAR deposition in sodium imaging is approximately four times that in proton imaging [165].

Due to the different resonance frequency respect to protons and the low SNR, dedicated hardware (multi-nuclei RF channel) and coils must be used for ^{23}Na imaging [166, 167].

As far as acquisition sequences are concerned, ultra-short echo times (UTE) are required for sufficient SNR and for avoiding strong T2*-weighting due to a fast biexponential transversal decay of sodium; in fact, ^{23}Na includes two T2* components: a fast component $T2_f^* \approx$ (0.5-4) ms and a slow component $T2_s^* \approx$ (15-30) ms [168, 169]. Most sodium heart measurements are performed with 2D [169] or 3D [165, 170-172] MRI sequences, with non-uniform sampling trajectories, increasing the SNR and reducing the acquisition time.

In [165], optimized sequence and sequence parameters are described, to allow three-dimensional (3D) sodium imaging of the entire human heart *in vivo*. A 3D stack of spirals sequence was acquired for imaging the entire human heart in about 6-10 minutes.

In a recent work [170], different 3D UTE sequences for anisotropic resolution in one direction were developed and investigated with respect to SNR efficiency, measurement time, and blurring behavior under the influence of the T2* decay; resulting data on ^{23}Na measurements of the human heart showed a reduction of acquisition time and an increase of SNR.

CONCLUSION

The advanced CMRI techniques described in this review provide a comprehensive assessment of the heart as a function of disease early detection and follow-up, thereby allowing unprecedented insight into the patho-physiology of the diverse cardiac diseases.

These new techniques are promising for their use in clinical practice and extend the already established role of CMR in the assessment of cardiovascular pathologies.

CONFLICT OF INTEREST

The authors confirm that this article content has no conflict of interest.

ACKNOWLEDGEMENTS

Declared none.

REFERENCES

[1] Motwani M, Kidambi A, Greenwood JP, *et al*. Advances in cardiovascular magnetic resonance in ischaemic heart disease and non-ischaemic cardiomyopathies. Heart 2014; 100: 1722-33.

[2] Andrew J, Ludman LCD, Petersen SE. CMR in Heart Failure: Current and Emerging Clinical Applications. Bentham Sci 2014; 3-40.

[3] Ghosn MG, Shah DJ. Important advances in technology and unique applications related to cardiac magnetic resonance imaging. Methodist Debakey Cardiovasc J 2014; 10: 159-62.

[4] Makowski MR, Botnar RM. MR imaging of the arterial vessel wall: molecular imaging from bench to bedside. Radiology 2013; 269: 34-51.

[5] Keegan J. Coronary artery wall imaging. J Magn Reson Imaging 2015; 41: 1190-202.

[6] Zhang S, Joseph AA, Voit D, *et al*. Real-time magnetic resonance imaging of cardiac function and flow-recent progress. Quant Imaging Med Surg 2014; 4: 313-29.

[7] Gutberlet M, Schwinge K, Freyhardt P, *et al*. Influence of high magnetic field strengths and parallel acquisition strategies on image quality in cardiac 2D CINE magnetic resonance imaging: comparison of 1.5 T vs. 3.0 T. Eur Radiol 2005; 15: 1586-97.

[8] Oshinski JN, Delfino JG, Sharma P, *et al*. Cardiovascular magnetic resonance at 3.0 T: current state of the art. J Cardiovasc Magn Reson 2010; 12: 55.

[9] Hays AG, Schär M, Kelle S. Clinical applications for cardiovascular magnetic resonance imaging at 3 Tesla. Curr Cardiol Rev 2009; 5: 237-42.

[10] Niendorf T, Sodickson DK, Krombach GA, *et al*. Toward cardiovascular MRI at 7 T: clinical needs, technical solutions and research promises. Eur Radiol 2010; 20: 2806-16.

[11] Niendorf T, Paul K, Oezerdem C, *et al*. W(h)ither human cardiac and body magnetic resonance at ultrahigh fields? technical advances, practical considerations, applications, and clinical opportunities. NMR Biomed 2015, doi: 10.1002/nbm.3268. [Epub ahead of print]

[12] Klix S, Els A, Paul K, *et al*. On the subjective acceptance during cardiovascular magnetic resonance imaging at 7.0 Tesla. PLoS One 2015; 10: e0117095.

[13] Niendorf T, Sodickson DK. Highly accelerated cardiovascular MR imaging using many channel technology: concepts and clinical applications. Eur Radiol 2008; 18: 87-102.

[14] Thalhammer C, Renz W, Winter L, *et al*. Two-dimensional sixteen channel transmit/receive coil array for cardiac MRI at 7.0 T: design, evaluation, and application. J Magn Reson Imaging 2012; 36: 847-57.

[15] Winter L, Kellman P, Renz W, *et al*. Comparison of three multichannel transmit/receive radiofrequency coil configurations for anatomic and functional cardiac MRI at 7.0T: implications for clinical imaging. Eur Radiol 2012; 22: 2211-20.

[16] Frauenrath T, Niendorf T, Kob M. Acoustic method for synchronization of Magnetic Resonance Imaging (MRI). Acta Acustica united with Acustica 2008: 148-55.

[17] Haacke EM, Brwon RW, Thonpson MR, Venkatesan R. Magnetic Resonance Imaging: Physical Principles and Sequence Design. John Wiley and Sons 1999.

[18] Tyler DJ, Hudsmith LE, Clarke K, Neubauer S, Robson MD. A comparison of cardiac (31)P MRS at 1.5 and 3 T. NMR Biomed 2008; 21: 793-8.

[19] Nayak KS, Cunningham CH, Santos JM, *et al*. Real-time cardiac MRI at 3 Tesla. Magn Reson Med 2004; 51: 655-660.

[20] Madelin G, Oesingmann N, Inglese M. Double Inversion Recovery MRI with fat suppression at 7 Tesla: initial experience. J Neuroimaging 2010; 20: 87-92.

[21] Markl M, Scherer S, Frydrychowicz A, *et al*. Balanced left ventricular myocardial SSFP-tagging at 1.5T and 3T. Magn Reson Med 2008; 60: 631-9.

[22] Hezel F, Thalhammer C, Waiczies S, *et al*. High spatial resolution and temporally resolved T2* mapping of normal human myocardium at 7.0 Tesla: an ultrahigh field magnetic resonance feasibility study. PLoS One 2012; 7: e52324.

[23] Niendorf T, Graessl A, Thalhammer C, *et al*. Progress and promises of human cardiac magnetic resonance at ultrahigh fields: a physics perspective. J Magn Reson 2013; 229: 208-22.

[24] Lattanzi R, Sodickson DK, Grant AK *et al*. Electrodynamic constraints on homogeneity and radiofrequency power deposition in multiple coil excitations. Magn Reson Med 2009; 61: 315-34.

[25] Zelinski AC, Angelone LM, Goyal VK *et al*. Specific absorption rate studies of the parallel transmission of inner-volume excitations at 7T. J Magn Reson Imaging 2008; 28: 1005-18.

[26] Schönberg S O, Baert AL, Dietrich O, *et al* . Parallel Imaging in Clinical MR Applications. Medical Radiology - diagnostic Imaging and Radiation Oncology. Ed. Schönberg S O, , Dietrich O, Reiser M F 2007, Springer.

[27] Snyder CJ, DelaBarre L, Metzger GJ, *et al*. Initial results of cardiac imaging at 7 Tesla, Magn. Reson. Med 2009; 61: 517-24.

[28] Dieringer M, Renz W, Lindel T, *et al*. Design and application of a four channel transmit/receive surface coil for functional cardiac imaging at 7 T, J. Magn. Reson. Imaging 2011; 33: 736-41.

[29] Thalhammer C, Renz W, Winter L, *et al*. Two-dimensional sixteen channel transmit/receive coil array for cardiac MRI at 7.0 T: design, evaluation, and application, J. Magn. Reson. Imaging 2012; 36: 847-57.

[30] Grassl A, Winter L, Thalhammer C, *et al*. Design, evaluation and application of an eight channel transmit/receive coil array for cardiac MRI at 7.0 T. Eur J Radiol 2013; 82: 752-9.

[31] Winter L, Kellman P, Renz W, *et al*. Comparison of three multichannel transmit/receive radiofrequency coil configurations for anatomic and functional cardiac MRI at 7.0 T: implications for clinical imaging. Eur Radiol 2012; 22: 2211-20.

[32] Katscher U, Bornert P, Leussler C, *et al*. Transmit SENSE. Magn Reson Med 2003; 49: 144-50.

[33] Van de Moortele PF, Akgun C, Adriany G, *et al*. B(1) destructive interferences and spatial phase patterns at 7T with a head transceiver array coil. Magn Reson Med 2205; 54: 1503-18.

[34] Gibiino F, Positano V, Wiesinger F, *et al*. Structured errors in reconstruction methods for Non-Cartesian MR data. Comput Biol Med 2013; 43: 2256-62.

[35] Gibiino F, Positano V, Landini L, *et al*. Regularization techniques on least squares non-uniform fast Fourier transform. Int J Numer Method Biomed Eng 2013; 29: 561-73.
[36] Donoho DL. Compressed sensing. IEEE Trans. Inf. Theory 2006; 52(4): 1289-306.
[37] Candès EJ, Romberg J, Tao T. Robust uncertainty principles: Exact signal reconstruction from highly incomplete frequency information. IEEE Trans Inf Theory 2006; 52(2): 489-509.
[38] Lustig M, Donoho D, Pauly JM. Sparse MRI: The application of compressed sensing for rapid MR imaging. Magnetic Resonance Med 2007; 58: 1182-95.
[39] Lustig M, Alley M. L 1 SPIR-iT: Autocalibrating Parallel Imaging Compressed Sensing. Proc Intl Soc Mag Reson Med 2009; 17: 379.
[40] Glassner A. An introduction to ray tracing. San Francisco, Calif: Morgan Kaufman, 1989.
[41] Valvano G, Martini N, Chiappino D, *et al*. Random Delayed Spirals for Compressive Sensing Cine MRI. Proc Intl Soc Mag Reson Med 2015; 23: 3633.
[42] Valvano G, Martini N, Landini L, *et al*. Variable Density Randomized Staco of Spirals (VDR-SoS) for Compressive Sensing MRI. Magnetic Resonance in Medicine 2015 (in press).
[43] Jung H, Ye JC, Kim EY. Improved k-t BLAST and k-t SENSE using FOCUSS. Phys Med Biol 2007; 52: 3201-26.
[44] Lustig M, Donoho DL, Santos JM, Pauly JM. Compressed sensing MRI. IEEE Signal Process Mag 2008; 25: 72-82.
[45] Pedersen H, Kozerke S, Ringgaard S, *et al*. k-t PCA: Temporally constrained k-t BLAST reconstruction using principal component analysis. Magn Reson Med 2009; 62: 706-16.
[46] Giese D, Wong J, Greil GF, *et al*. Towards highly accelerated Cartesian time-resolved 3D flow cardiovascular magnetic resonance in the clinical setting. J Cardiovasc Magn Reson 2014; 18: 16-42.
[47] Stoeck CT, Manka R, Boesiger P, *et al*. Undersampled cine 3D tagging for rapid assessment of cardiac motion. J Cardiovasc Magn Reson 2012; 14: 60.
[48] Schmidt J F M, Wissmann L, Manka R, Kozerke S. Iterative k-t principal component analysis with nonrigid motion correction for dynamic three-dimensional cardiac perfusion imaging. Magn Reson Med 2014; 72: 68-79.
[49] Zhao B, Haldar JP, Christodoulou AG, Liang ZP. Image reconstruction from highly undersampled (k, t)-space data with joint partial separability and sparsity constraints. IEEE Trans Med Imag 2012 31: 1809-20.
[50] Goud Lingala S, Hu Y, DiBella E, *et al*. Accelerated dynamic MRI exploiting sparsity and low-rank structure: k-t SLR. IEEE Trans Med Imag 2011; 30: 1042-54.
[51] Trémoulhéac B, Dikaios N, Atkinson D, *et al*. Dynamic MR image reconstruction-separation from undersampled (k,t)-space via low-rank plus sparse prior. IEEE Trans Med Imaging 2014; 33: 1689-701.
[52] Liang D, Liu B, Wang J, Ying L. Accelerating SENSE using compressed sensing. Magnetic Resonance Med 2009; 62: 1574-84.
[53] Otazo R, Kim D, Axel L, Sodickson DK. Combination of compressed sensing and parallel imaging for highly accelerated first-pass cardiac perfusion MRI. Magnetic Resonance Med 2010; 64: 767-76.
[54] Lustig M, Pauly JM. SPIRiT: Iterative self-consistent parallel imaging reconstruction from arbitrary kspace. Magnetic Resonance Med 2010; 64: 457-71.
[55] Pawar K, Egan G, Zhang J. Multichannel compressive sensing MRI using noiselet encoding. PLoS One 2015; 10: e0126386.
[56] Binter C, Ramb R, Jung B, *et al*. A g-factor metric for k-t SENSE and k-t PCA based parallel imaging. Magn Reson Med 2015 doi: 10.1002/mrm.25606. [Epub ahead of print]
[57] Christodoulou AG, Zhang H, Zhao B, *et al*. High-resolution cardiovascular MRI by integrating parallel imaging with low-rank and sparse modeling. IEEE Trans Biomed Eng 2013; 60: 3083-92.
[58] Salerno M, Kramer CM. Advances in Parametric Mapping with CMR Imaging. JACC Cardiovasc Imaging 2013; 6: 806-22
[59] Sado DM, Maestrini V, Piechnik SK, *et al*. Noncontrast myocardial T1 mapping using cardiovascular magnetic resonance for iron overload. J Magn Reson Imaging 2015; 41: 1505-11.
[60] Sado DM, White SK ,Piechnik SK, *et al*. Identification and assessment of Anderson-Fabry disease by cardiovascular magnetic resonance noncontrast myocardial T1 mapping. Circ Cardiovasc Imaging 2013; 6: 392-8.
[61] Messroghli DR, Walters K, Plein S, *et al*. Myocardial T1 mapping: application to patients with acute and chronic myocardial infarction. Magn Reson Med 2007; 58: 34-40.
[62] Ferreira VM, Piechnik SK, Dall'Armellina E, *et al*. T1 mapping for the diagnosis of acute myocarditis using CMR: comparison to T2-weighted and late gadolinium enhanced imaging. JACC Cardiovasc Imaging 2013; 6: 1048-58.
[63] Karamitsos TD, Piechnik SK, Banypersad SM, *et al*. Noncontrast T1 mapping for the diagnosis of cardiac amyloidosis. JACC Cardiovasc Imaging 2013; 6: 488-97.
[64] Bulluck H, Maestrini V, Rosmini S, *et al*. Myocardial T1 mapping. Circ J 2015; 79: 487-94.
[65] White SK, Sado DM, Fontana M, *et al*. T1 mapping for myocardial extracellular volume measurement by CMR: bolus only versus primed infusion technique. JACC Cardiovasc Imaging 2013; 6: 955-62.
[66] Kellman P, Wilson JR, Xue H, *et al*. Extracellular volume fraction mapping in the myocardium, part 2: initial clinical experience. J Cardiovasc Magn Reson 2012; 14: 64.
[67] Messroghli DR, Radjenovic A, Kozerke S, *et al*. Modified Look-Locker inversion recovery (MOLLI) for high-resolution T1 mapping of the heart. Magn Reson Med 2004; 52: 141-6.
[68] Nekolla S, Gneiting T, Syha J, *et al*. T1 maps by K-space reduced snapshot-FLASH MRI.', J Comput Assist Tomogr 1992; 16: 327-32.
[69] Xue H, Greiser A, Zuehlsdorff S, *et al*. Phase-sensitive inversion recovery for myocardial T1 mapping with motion correction and parametric fitting. Magn Reson Med 2013; 69: 1408-20.
[70] Xue H, Shah S, Greiser A, *et al*. Motion correction for myocardial T1 mapping using image registration with synthetic image estimation. Magn Reson in Med 2012; 67: 1644-55.
[71] Piechnik SK, Ferreira VM, Dall'Armellina E, *et al*. Shortened Modified Look-Locker Inversion recovery (ShMOLLI) for clinical myocardial T1-mapping at 1.5 and 3 T within a 9 heartbeat breathhold. J Cardiovasc Magn Reson 2010; 12: 69.
[72] Messroghli DR, Greiser A, Fröhlich M, *et al*. Optimization and validation of a fully-integrated pulse sequence for modified look-locker inversion-recovery (MOLLI) T1 mapping of the heart. J Magn Reson Imaging 2007; 26: 1081-6.
[73] Salerno M, Janardhanan R, Jiji RS. Comparison of methods for determining the partition coefficient of gadolinium in the myocardium using T1 mapping. J Magn Reson Imaging 2013; 38: 217-24.
[74] Chow K, Flewitt JA, Green JD. Saturation recovery single-shot acquisition (SASHA) for myocardial T1 mapping. Magn Reson Med 2013; 71: 2082-95.
[75] Weingärtner S, Akçakaya M, Basha T. Combined saturation/inversion recovery sequences for improved evaluation of scar and diffuse fibrosis in patients with arrhythmia or heart rate variability. Magn Reson Med 2014; 71: 1024-34.
[76] Kellman P and Hansen MS. T1-mapping in the heart: accuracy and precision. J Cardiovasc Magn Reson 2014; 16: 2.
[77] Higgins D, Moon J. Review of T1 Mapping Methods: Comparative Effectiveness Including Reproducibility Issues. Curr Cardiovascular Imaging Reports 2014; 7: 9252
[78] Roujol S, Weingärtner S, Foppa M, *et al*. Accuracy, precision, and reproducibility of four T1 mapping sequences: a head-to-head comparison of MOLLI, ShMOLLI, SASHA, and SAPPHIRE. Radiology 2014; 272: 683-9.
[79] Moon JC, Messroghli DR, Kellman P, *et al*. Myocardial T1 mapping and extracellular volume quantification: a Society for Cardiovascular Magnetic Resonance (SCMR) and CMR Working Group of the European Society of Cardiology consensus statement. J Cardiovasc Magn Reson 2013; 15: 92.
[80] Fontana M, White SK, Banypersad SM, *et al*. Comparison of T1 mapping techniques for ECV quantification. Histological validation and reproducibility of ShMOLLI versus multibreath-hold T1 quantification equilibrium contrast CMR. J Cardiovasc Magn Reson 2012; 14: 88.
[81] Sibley CT, Noureldin RA, Gai N, *et al*. T1 Mapping in cardiomyopathy at cardiac MR: comparison with endomyocardial biopsy. Radiology 2012; 265: 724-732.
[82] de Meester de Ravenstein C, Bouzin C, Lazam S, *et al*. Histological Validation of measurement of diffuse interstitial myocardial fibrosis by myocardial extravascular volume fraction from Modified Look-Locker imaging (MOLLI) T1 mapping at 3T. J Cardiovasc Magn Reson 2015; 17: 48.

[83] Ambale-Venkatesh B and Lima JAC. Cardiac MRI: a central prognostic tool in myocardial fibrosis. Nat Rev Cardiol 2015; 12: 18-29.
[84] Ramazzotti A, Pepe A, Positano V. Multicenter validation of the magnetic resonance T2* technique for segmental and global quantification of myocardial iron. J Magn Reson Imaging 2009; 30: 62-8.
[85] Positano V, Pepe A, Santarelli MF, *et al*. Standardized T2* map of normal human heart *in vivo* to correct T2* segmental artefacts. NMR Biomed 2007; 20: 578-90.
[86] Positano V, Pepe A, Santarelli MF, *et al*. Multislice multiecho T2* cardiac magnetic resonance for the detection of heterogeneous myocardial iron distribution in thalassaemia patients. NMR Biomed 2009; 22: 707-15.
[87] Meloni A, Positano V, Ruffo GB, *et al*. Improvement of heart iron with preserved patterns of iron store by CMR-guided chelation therapy. Eur Heart J Cardiovasc Imaging 2015; 16: 325-34
[88] Positano V, Meloni A, Santarelli MF, *et al*. Fast generation of T2* maps in the entire range of clinical interest: application to thalassemia major patients. Comput Biol Med 2015; 56: 200-10
[89] Meloni A, Zmyewski H, Rienhoff Jr HY, *et al*. Fast approximation to pixel wise relaxivity maps: validation in iron overloaded subjects. J. Magn. Reson. Imaging 2013; 31: 1074-80.
[90] Zia MI, Ghugre NR, Connelly KA, *et al*. Characterizing myocardial edema and hemorrhage using quantitative T2 and T2* mapping at multiple time intervals post ST-segment elevation myocardial infarction. Circ Cardiovasc Imaging 2012; 5: 566-72.
[91] Manka R, Paetsch I, Schnackenburg B, *et al*. BOLD cardiovascular magnetic resonance at 3.0 Tesla in myocardial ischemia. J Cardiovasc Magn Reson 2010; 12: 54.
[92] Meloni A, Positano V, Keilberg P, *et al*. Feasibility, reproducibility, and reliability for the T2* iron evaluation at 3 T in comparison with 1.5 T. Magn Reson Med 2012; 68: 543-51.
[93] Meloni A, Hezel F, Positano V *et al*. Detailing magnetic field strength dependence and segmental artifact distribution of myocardial effective transverse relaxation rate at 1.5, 3.0, and 7.0 T. Magn Reson Med 2014; 71: 2224-30
[94] Foltz WD, Al-Kwifi O, Sussman MS, *et al*. Optimized spiral imaging for measurement of myocardial T2 relaxation. Magn Reson Med 2003; 49: 1089-97.
[95] Huang TY, Liu YJ, Stemmer A, *et al*. T2 measurement of the human myocardium using a T2-prepared transient-state TrueFISP sequence. Magn Reson Med 2007; 57: 960-6.
[96] Gibiino F, Lechner-Greite S, Schirmer T, *et al*. Effects of inner volume field-of-view reduction on myocardial T2 mapping. J Magn Reson Imaging 2015; 42: 175-9.
[97] Giri S, Chung YC, Merchant A, *et al*. T2 quantification for improved detection of myocardial edema. J Cardiovasc Magn Reson 2009; 11: 56.
[98] He T, Smith GC, Gatehouse PD, *et al*. On using T2 to assess extrinsic magnetic field inhomogeneity effects on T2* measurements in myocardial siderosis in thalassemia. Magn Reson Med 2009; 61: 501-16.
[99] Shehata ML, Cheng S, Osman NF, *et al*. Myocardial tissue tagging with cardiovascular magnetic resonance. J Cardiovasc Magn Reson 2009; 11: 55
[100] Zerhouni EA, Parish DM, Rogers WJ, *et al*. Human heart: tagging with MR imaging--a method for noninvasive assessment of myocardial motion. Radiology 1988; 169: 59-63.
[101] Axel L, Dougherty L. MR imaging of motion with spatial modulation of magnetization. Radiology 1989; 171: 841-5.
[102] Sodickson DK, Manning WJ: Simultaneous acquisition of spatial harmonics (SMASH): fast imaging with radiofrequency coil arrays. Magn Reson Med 1997; 38: 591-603.
[103] Pruessmann KP, Weiger M, Scheidegger MB, *et al*. SENSE: sensitivity encoding for fast MRI. Magn Reson Med 1999; 42: 952-62.
[104] El-Sayed H Ibrahim. Myocardial tagging by Cardiovascular Magnetic Resonance: evolution of techniques-pulse sequences, analysis algorithms, and applications. Journal of Cardiovascular Magnetic Resonance 2011, 13,36: 2-40.
[105] Jeung MY, Germain P, Croisille P, El Ghannudi S, Roy C, Gangi A. Myocardial Tagging with MR Imaging: Overview of Normal and Pathologic Findings, PhD RadioGraphics 2012; 32: 1381-98
[106] Kramer U, Deshpande V, Fenchel M, *et al*. Cardiac MR tagging: optimization of sequence parameters and comparison at 1.5 T and 3.0 T in a volunteer study. Rofo 2006; 178: 515-24.
[107] Guttman MA, Prince JL, McVeigh ER. Tag and contour detection in tagged MR images of the left ventricle. IEEE Trans Med Imaging 1994; 13: 74-88.
[108] Axel L, Goncalves RC, Bloomgarden D. Regional heart wall motion: two-dimensional analysis and functional imaging with MR imaging. Radiology 1992; 183: 745-50.
[109] Osman NF, McVeigh ER, Prince JL. Imaging heart motion using armonic phase MRI. IEEE Trans Med Imaging 2000; 19: 186-202.
[110] Pan L, Prince JL, Lima JA, *et al*. Fast tracking of cardiac motion using 3D-HARP. IEEE Trans Biomed Eng 2005; 52: 1425-1435.
[111] Castillo E, Osman NF, Rosen BD, *et al*. Quantitative assessment of regional myocardial function with MR-tagging in a multicenter study: interobserver and intraobserver agreement of fast strain analysis with Harmonic Phase (HARP) MRI. J Cardiovasc Magn Reson 2005, 7: 783-91.
[112] Pingitore A1, Lombardi M, Scattini B, *et al*. Head to head comparison between perfusion and function during accelerated high-dose dipyridamole magnetic resonance stress for the detection of coronary artery disease. Am J Cardiol 2008; 101: 8-14
[113] Masci PG, Marinelli M, Piacenti M, *et al*. Myocardial structural, perfusion, and metabolic correlates of left bundle branch block mechanical derangement in patients with dilated cardiomyopathy. A tagged cardiac magnetic resonance and positron emission tomography Study. Circ. Cardiovasc Imaging 2010; 3: 482-90.
[114] Markl M, Frydrychowicz A, Kozerke S, *et al*. 4D flow MRI. J Magn Reson Imaging 2012; 36: 1015-36.
[115] Stankovic Z, Allen BD, Garcia J, *et al*. 4D flow imaging with MRI. Cardiovasc Diagn Ther 2014; 4: 173-92.
[116] Carlsson M, Töger J, Kanski M, *et al*. Quantification and visualization of cardiovascular 4D velocity mapping accelerated with parallel imaging or k-t BLAST: head to head comparison and validation at 1.5 T and 3 T. J Cardiovasc Magn Reson 2011; 13: 55.
[117] Zaman A, Motwani M, Oliver JJ, *et al*. 3.0T, time-resolved, 3D flow-sensitive MR in the thoracic aorta: Impact of k-t BLAST acceleration using 8- versus 32-channel coil arrays. J Magn Reson Imaging 2014, DOI: 10.1002/jmri.24814.
[118] Gu T, Korosec F, R Block, *et al*. PC VIPR: a high-speed 3D phase-contrast method for flow quantification and high-resolution angiography. AJNR Am J Neuroradiol 2005: 26: 743-9.
[119] Petersson S, Sigfridsson A, Dyverfeldt P, *et al*. Retrospectively gated intracardiac 4D flow MRI using spiral trajectories. Magn Reson Med 2015, DOI: 10.1002/mrm.25612.
[120] van Ooij P, Semaan E, Schnell S *et al*. Improved respiratory navigator gating for thoracic 4D flow MRI. Magn Reson Imaging 2015, DOI: 10.1016/j.mri.2015.04.008.
[121] Uribe S, Beerbaum P, Sørensen TS, *et al*. Four-dimensional (4D) flow of the whole heart and great vessels using real-time respiratory self-gating. Magn Reson Med 2009; 62: 984-992.
[122] Valverde I, Simpson J, Schaeffter T, *et al*. 4D phase-contrast flow cardiovascular magnetic resonance: comprehensive quantification and visualization of flow dynamics in atrial septal defect and partial anomalous pulmonary venous return. Pediatr Cardiol 2010; 31: 1244-8.
[123] Lorenz R, Bock J, Barker AJ, *et al*. 4D flow magnetic resonance imaging in bicuspid aortic valve disease demonstrates altered distribution of aortic blood flow helicity. Magn Reson Med 2014; 71: 1542-53.
[124] Mahadevia R, Barker AJ, Schnell S, *et al*. Bicuspid aortic cusp fusion morphology alters aortic three-dimensional outflow patterns, wall shear stress, and expression of aortopathy. Circulation 2014; 129: 673-82.
[125] Stalder AF, Russe MF, Frydrychowicz A, *et al*. Quantitative 2D and 3D phase contrast MRI: optimized analysis of blood flow and vessel wall parameters. Magn Reson Med 2008; 60: 1218-31.
[126] Wentland L, Wieben O, François CJ *et al*. Aortic pulse wave velocity measurements with undersampled 4D flow-sensitive MRI: comparison with 2D and algorithm determination. J Magn Reson Imaging 2013; 37: 853-9.
[127] Rengier F, Delles M, Eichhorn J, *et al*. Noninvasive 4D pressure difference mapping derived from 4D flow MRI in patients with repaired aortic coarctation: comparison with young healthy volunteers. Int J Cardiovasc Imaging 2015; 31: 823-30.
[128] Barker AJ, van Ooij P, Bandi K, *et al*. Viscous energy loss in the presence of abnormal aortic flow. Magn Reson Med 2014; 72: 620-628.

[129] Entezari P, Schnell S, Mahadevia R *et al*. From unicuspid to quadricuspid: Influence of aortic valve morphology on aortic three-dimensional hemodynamics. J Magn Reson Imaging 2014; 40: 1342-6.

[130] Garcia J, Markl M, Schnell S, *et al*. Evaluation of aortic stenosis severity using 4D flow jet shear layer detection for the measurement of valve effective orifice area. Magn Reson Imaging 2014; 32: 891-8.

[131] Hope MD, Meadows AK, Hope TA, *et al*. Clinical evaluation of aortic coarctation with 4D flow MR imaging. J Magn Reson Imaging 2010; 31: 711-8.

[132] Clough RE, Waltham M, Giese D, *et al*. A new imaging method for assessment of aortic dissection using four-dimensional phase contrast magnetic resonance imaging. J Vasc Surg 2012; 55: 914-23.

[133] Santarelli MF, Martini N, Positano V, *et al*. Models and methods in cardiac imaging for metabolism studies. Curr Pharm Des 2014; 20: 6171-81.

[134] van Ewijk PA, Schrauwen-Hinderling VB, Bekkers SC, *et al*. MRS: a noninvasive window into cardiac metabolism. NMR Biomed 2015; 28: 747-66

[135] Weiss K, Martini N, Boesiger P, *et al*. Cardiac proton spectroscopy using large coil arrays. NMR Biomed 2013; 26: 276-84.

[136] Weiss K, Martini N, Boesiger P, *et al*. Metabolic MR imaging of regional triglyceride and creatine content in the human heart. Magn Reson Med 2012; 68: 1696-1704.

[137] Pohmann R, von Kienlin M, Haase A. Theoretical evaluation and comparison of fast chemical shift imaging methods. J Magn Reson 1997; 129: 145-60.

[138] Giovannetti G, Hartwig V, Frijia F, *et al*. Hyperpolarized 13C MRS cardiac metabolism studies in pigs: comparison between surface and volume radiofrequency coils. Appl Magn Reson 2012; 42: 413-28.

[139] Giovannetti G, Frijia F, Hartwig V, *et al*. Design of a quadrature surface coil for Hyperpolarized 13C MRS cardiac metabolism studies in pigs. Concepts in Magnetic Resonance Part B 2013; 43(B): 69-77.

[140] Giovannetti G, Frijia F, Menichetti L, *et al*. Hyperpolarized 13C MRS surface coil: design and signal-to-noise ratio estimation. Med Phys 2010; 37: 5361-9.

[141] Dominguez-Viqueira W, Lau AZ, Chen AP, *et al*. Multichannel receiver coils for improved coverage in cardiac metabolic imaging using prepolarized 13C substrates. Magn Reson Med 2013; 70: 295-300.

[142] Shin PJ, Larson PEZ, Uecker M, *et al*. Chemical shift separation with controlled aliasing for hyperpolarized (13) C metabolic imaging. Magn Reson Med 2014; Epub ahead of print in Wiley Online Library doi: 10.1002/mrm.25473.

[143] Szczepaniak LS, Dobbins RL, Metzger GJ, *et al*. Myocardial triglycerides and systolic function in humans: *in vivo* evaluation by localized proton spectroscopy and cardiac imaging. Magn Reson Med 2003; 49: 417-23.

[144] Bottomley PA, Weiss RG. Non-invasive magnetic-resonance detection of creatine depletion in non-viable infarcted myocardium. The Lancet 1998; 351(9104): 714-8.

[145] Martini N, Santarelli MF, Giovannetti G, *et al*. Noise correlations and SNR in phased-array MRS. NMR Biomed 2010; 23: 66-73.

[146] van der Meer RW, Doornbos J, Kozerke S, *et al*. Metabolic imaging of myocardial triglyceride content: reproducibility of 1H MR spectroscopy with respiratory navigator gating in volunteers. Radiology 2007; 245: 251-7

[147] Schär M, Kozerke S and Boesiger P. Navigator gating and volume tracking for double-triggered cardiac proton spectroscopy at 3 Tesla. Magn Reson Med 2004; 51: 1091-5.

[148] Neubauer S, Horn M, Hahn D, Kochsiek KT. Clinical cardiac magnetic resonance spectroscopy: present state and future directions. Mol. Cell. Biochem. 1998; 184: 439-43.

[149] Lamb HJ, Doornbos J, den Hollander JA, *et al*. Reproducibility of human cardiac 31P-NMR spectroscopy. NMR Biomed, 1996; 9: 217-27.

[150] Von Kienlin M, Mejia R. Spectral localization with optimal point-spread function. J Magn Reson 1991; 94: 268-87.

[151] Löffler R, Sauter R, Kolem H, *et al*. Localized spectroscopy from anatomically matched compartments: improved sensitivity and localization for cardiac 31P MRS in humans. J Magn Reson 1998; 134: 287-99.

[152] Santarelli MF, Positano V, Menichetti L, *et al*. Cardiovascular molecular imaging: new methodological strategies. Curr Pharm Des 2013; 19: 2439-46.

[153] Schroeder MA, Atherton HJ, Ball DR, *et al*. Real-time assessment of Krebs cycle metabolism using hyperpolarized 13C magnetic resonance spectroscopy. FASEB J 2009; 23: 2529-8.

[154] Rider OJ, Tyler DJ. Clinical implications of cardiac hyperpolarizedmagnetic resonance imaging. J. Cardiovasc. Magn. Reson 2013; 15: 93.

[155] Tyler DJ, Schroeder MA, Cochlin LE, Clarke K, Radda GK. Application of hyperpolarized magnetic resonance in the study of cardiac metabolism. Appl Magn Reson 2008; 34: 523-31.

[156] Aquaro GD, Menichetti L. Hyperpolarized 13C-magnetic resonance spectroscopy: are we ready for metabolic imaging? Circ Cardiovasc Imaging 2014; 7: 854-6.

[157] Ardenkjaer-Larsen JH, Fridlund B, Gram A, *et al*. Increase in signal-to-noise ratio of>10,000 times in liquid-state NMR. Proc Natl Acad Sci USA 2003; 100(10): 158-63.

[158] Menichetti L, Frijia F, Flori A, *et al*. Assessment of real-time myocardial uptake and enzymatic conversion of hyperpolarized [1-^{13}C]pyruvate in pigs using slice selective magnetic resonance spectroscopy. Contrast Media Mol Imaging 2012; 7: 85-94.

[159] Santarelli MF, Positano V, Giovannetti G, *et al*. How the signal-to-noise ratio influences hyperpolarized 13C dynamic MRS data fitting and parameter estimation. NMR Biomed 2012; 25: 925-34.

[160] Flori A, Liserani M, Frijia F, *et al*. Real-time cardiac metabolism assessed with hyperpolarized [1-(13) C]acetate in a large-animal model. Contrast Media Mol Imaging 2015; 10: 194-202.

[161] Chen AP, Lau JYC, Alvares RDA, *et al*. Using [1-(13) C]lactic acid for hyperpolarized (13) C MR cardiac studies. Magn Reson Med 2015; 73: 2087-93.

[162] Aquaro G D, Frijia F, Positano V, *et al*. Three-dimensional magnetic resonance mapping of cardiac metabolism by hyperpolarized 13C-pyruvate in a pig model of ischemia-reperfusion. JAAC: Cardiovascular Imaging 2013; 6: 743-4.

[163] Dodd M S, Atherton HJ, Carr CA, *et al*. Impaired *in vivo* mitochondrial Krebs cycle activity after myocardial infarction assessed using hyperpolarized magnetic resonance spectroscopy. Circ Cardiovasc Imaging 2014; 7: 895-904.

[164] Bottomley PA. Sodium MRI in human heart: a review. NMR Biomed 2015; Epub ahead of print in Wiley Online Library. doi: 10.1002/nbm.3265

[165] Gai ND, Rochitte C, Nacif MS, Bluemke DA. Optimized three-dimensional sodium imaging of the human heart on a clinical 3T scanner. Magn Reson Med, Imaging Sciences, National Institutes of Health, Bethesda USA 2015; 73: 623-32.

[166] Giovannetti G, Pingitore A, Positano V, *et al*. Improving sodium Magnetic Resonance in humans by design of a dedicated 23Na surface coil. Measurement 2014; 50: 285-92.

[167] Ouwerkerk R, Weiss RG, Bottomley PA. Measuring human cardiac tissue sodium concentrations using surface coils, adiabatic excitation, and twisted projection imaging with minimal T2 losses. J Magn Reson Imaging 2005; 21: 546-555.

[168] Constantinides CD, Gillen JS, Boada FE, *et al*. Human skeletal muscle: sodium MR imaging and quantification potential applications in exercise and disease. Radiology 2000; 216: 559-68.

[169] Konstandin S, Schad LR. Two-dimensional radial sodium heart MRI using variable-rate selective excitation and retrospective electrocardiogram gating with golden angle increments. Magn Reson Med 2013; 70: 791-9.

[170] Konstandin S, Krämer P, Günther M, Schad LR. Sodium magnetic resonance imaging using ultra-short echo time sequences with anisotropic resolution and uniform k-space sampling. Magn Reson Imaging 2015; 33: 319-27.

[171] Nagel AM, Laun FB, Weber MA, Matthies C, Semmler W, Schad LR. Sodium MRI using a density-adapted 3D radial acquisition technique. Magn Reson Med 2009; 62: 1565-73.

[172] Konstandin S, Nagel AM. Measurement techniques for magnetic resonance imaging of fast relaxing nuclei. Magn Reson Mater Phys 2014; 27: 5-19.

Received: July 19, 2015 **Accepted: November 5, 2015**